



Cite this: DOI: 10.1039/c6cp04359c

Rotation measurements of a thermally driven rotary nanomotor with a spring wing†

Kun Cai,^{ab} Jingzhou Yu,^a Lingnan Liu,^a Jiao Shi^a and Qing H. Qin^{*b}

Due to the extremely small dimensions and super high frequency of the rotor in a thermally driven rotary nanomotor made from carbon nanostructures, measuring the rotational frequency of the nanomotor is still an open issue. To this end, a measuring system is constructed in which a spring wing is connected with the rotor to provide collisions with a probe tip whose deflection reflects the rotational frequency of the rotor. The spring wing is formed by connecting an end-tube from a carbon nanotube and a graphene with differently hydrogenated surfaces. Due to the alternative hydrogenation of the two surfaces, the graphene shrinks like a spring. When the rotational frequency increases, the centrifugal force applied on the wing increases and then the spring is stretched (becoming longer). As the end-tube rotates with the rotor and reaches the probe tip, a collision occurs between the end-tube and the probe tip. After collision, the probe tip undergoes a variation of vertical deflection that can be measured through atomic force microscopy. The relation between the maximal deflection of the probe tip and the rotational frequency of the rotor is determined via numerical experiments. The effects of the configuration (namely hydrogenation and length) of graphene on the rotation of the rotor are investigated. The results provide some insight into the fabrication of nanomachines.

Received 22nd June 2016,
Accepted 21st July 2016

DOI: 10.1039/c6cp04359c

www.rsc.org/pccp

1. Introduction

Carbon nanotubes and few-layer graphene (GN) are typical low dimensional materials. Due to their excellent physical properties, these low dimensional materials have attracted much attention from researchers since they were discovered and fabricated.^{1,2} Among the properties of these carbon nanostructures,^{2–6} their mechanical behaviors, including super high modulus,⁴ flexibility,^{7,8} and superlubricity^{8,9} among neighbor tubes or neighbor layers, demonstrate their great potential application in the design of nanodevices^{10–13} with high robustness.

Among the nanodevices fabricated from carbon nanostructures, nanomotors play an important role in nano-electromechanical systems (NEMS).^{14,15} According to the motion style, nanomotors can be classified into two major types. In the linear nanomotor,^{16,17} the mover has a translational motion on the stator. It is usually known as an oscillator^{8,18,19} when the mover oscillates periodically on the stator. The other type is known as a rotary nanomotor,^{16,20–27} in which the rotor has a rotation along the axis of the stator.

A typical rotary nanomotor made from a carbon nanostructure was reported in the work of Fennimore *et al.*,²⁰ in which multi-walled carbon nanotubes (MWNTs) acted as a bearing. The rotation of the rotor on the nanobearing is actuated by an external electric field. By applying an external electric field onto a double-walled nanotube system, Tu and Hu²² investigated the mechanical motion of the outer tube along the axis of the long inner tube of the system. Wang *et al.*²³ designed an electron tunneling-driven rotary nanomotor in which fullerene blades were charged/discharged periodically and driven to rotate. Hamdi *et al.*²⁵ investigated the inter-tube screw-like motion of nanotubes in a rotary nanomotor that had two axially aligned, opposing chirality nanotube shuttles. Diverging from the electric field driven approach, Kang and Hwang²¹ investigated the dynamic response of a nanofluid-driven carbon-nanotube motor made from MWNTs. Similarly, Prokop *et al.*²⁴ adopted gas flow to drive a rotary molecular motor. It should be noted that these systems are usually very complex, due to the requirement for many auxiliaries that hampered miniaturization or nanofabrication. A temperature field can also be used to drive the motion of a nanocomponent. In experiments on a nanocargo system constructed from MWNTs, Barreiro *et al.*¹⁶ found the rotation and translational motion of the outer tube along the axis of the inner tube when a thermal gradient existed along the axis of the inner tube. In a study of the dynamic behavior of double-walled carbon nanotubes (DWNTs) at a canonical *NVT* ensemble, Cai *et al.*²⁶ found that the rotation of the inner tube in a fixed

^a College of Water Resources and Architectural Engineering, Northwest A&F University, Yangling, 712100, China

^b Research School of Engineering, the Australian National University, Acton, 2600, ACT, Australia. E-mail: qinghua.qin@anu.edu.au

† Electronic supplementary information (ESI) available: Movie 1. [$N_t = N_b = 4$] [$L = 8.8$ nm] in [2000, 2500] ps.avi. Movie 2. [$N_t = N_b = 4$] [$L = 10.5$ nm] in [200, 700] ps.avi. Movie 3. [$N_t = N_b = 2$] [$L = 9.4$ nm] in [11 000, 11 500] ps.avi. Movie 4. [$N_t = N_b = 2$] [$L = 10.25$ nm] in [11 000, 11 500] ps.avi. See DOI: 10.1039/c6cp04359c

outer tube could be driven by a gradientless temperature field. The mechanism was recently further revealed by Cai *et al.*²⁷ The rotation of the rotor is due to the collision between the end carbon atoms on the rotor and stator with respect to thermal vibration of the atoms. As the layout of the end carbon atoms on the stator has rotary symmetry, the collision provides axial torque that is proportional to the rotational acceleration of the rotor. In simulation, the rotational velocity of the rotor becomes increasingly obvious and stable as the friction between the rotor and stator balances the torque. Hence, the nanomotor is known as a thermally driven rotary nanomotor (TDRM). From numerical experiments, the rotational frequency of the rotor can be over 200 GHz. As the rotor has very small dimensions, the rotation of the TDRM cannot be observed using traditional instrumentation such as *in situ* microscopy. To test the rotational frequency in the potential fabrication of a nanomotor, we suggest the use of a probe test method (see Fig. 1). In the method, the rotor is connected with a wing from an end-tube and a hydrogenated GN nanoribbon. Before rotation, the GN shrinks to become a spring, and the distance between the end-tube and the probe tip⁹ is large enough to avoid interaction between them. As the rotational frequency of the rotor increases, the “spring” wing unfolds due to the centrifugal effect, and collision between the end-tube and probe tip can occur. When the deflection of the probe tip is determined, we can calculate the rotational frequency of the rotor. Details of the calculations are given in Section 3.

2. Models and methodology

In this study, the system shown in Fig. 1a and b is adopted. In the analysis, L , L^* and the C-H layout schemes (*i.e.*, $N_t = N_b$) may have different values. The remaining geometric parameters are fixed. The number of hydrogen atoms depends on the length of HGN only, rather than on the value of N_t and N_b .

The open source of the molecular dynamic package LAMMPS is employed for the numerical experiments.²⁸ The time step is set at 0.001 ps in the analysis. Before simulation, energy minimization for the system is carried out using the steepest descending algorithm. After energy minimization on the initial model, the atoms (including inward radial deviated (IRD) atoms, see Fig. 1c) on the two stators are fixed. The rotor and two stators form the simplest thermal driven nanomotor. The inward radial deviations of the IRD atoms are equal to 0.4 times the C-C bond length (0.142 nm). Due to the smaller distance between the IRD atoms and the inner tube, the thermal-vibration-based collision between the atoms on the rotor and the IRD atoms will be far stronger than that between the other atoms on the stators and the rotor. Hence, the rotation of rotor is accelerated efficiently as the IRD atoms are layout axisymmetric. Next, the system is put in an *NVT* ensemble (the Nosé–Hoover thermostat, $T = 300$ K) with a damping constant of 0.1 ps. After 50 ps of relaxation, the dynamic responses of the system are computed in an *NVT* ensemble at 300 K. At 300 K, the rotor will be driven to rotate

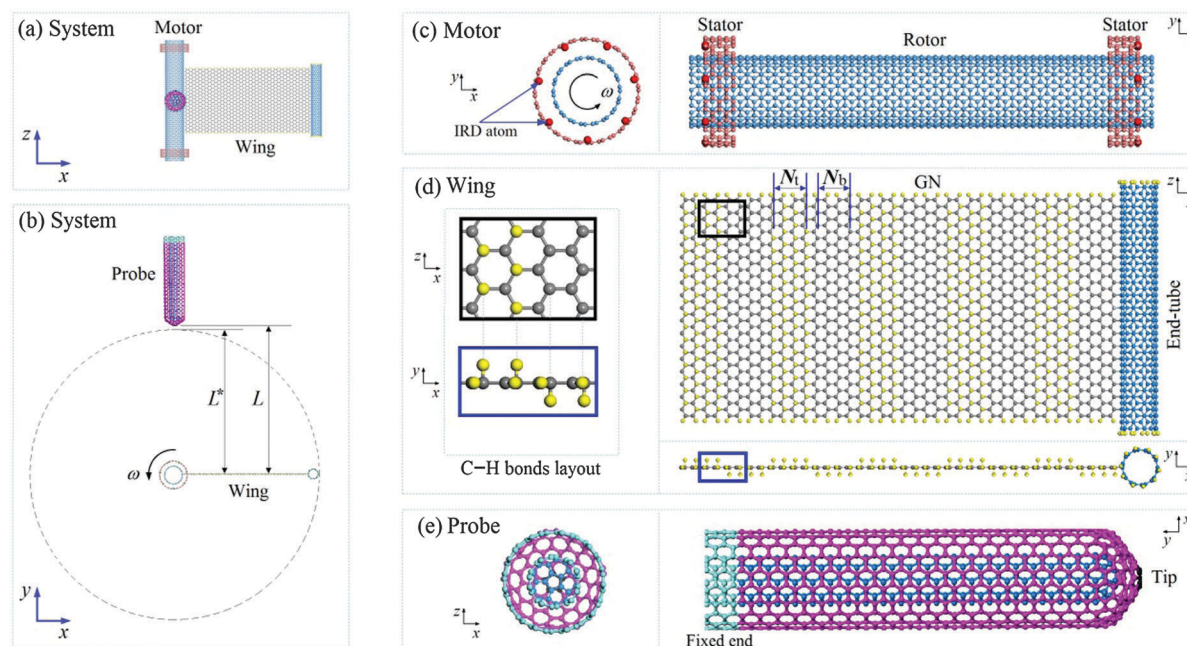


Fig. 1 Schematic of a thermally driven rotary nanosystem (a and b) with a motor (c)²⁷ and a cantilever probe (e). The nanomotor contains a complex rotating part made from a hydrogenated graphene (HGN)³⁰ connecting a centre-tube and an end-tube. (d) On the wing (HGN + end-tube), each edge carbon atom is bonded with a hydrogen atom (yellow). For the inner carbon atoms in the HGN, the layout of C-H bonds is shown in (d). “ N_t ” and “ N_b ” are the number of lines of C-H bonds on the top and bottom surfaces ($x-z$ plane) of the HGN, respectively. In this model, $N_t = N_b = 4$. In the present study, N_t and N_b are always identical in the main part of the GN, *i.e.*, $N_t = N_b$. (e) The probe is constructed from capped double-walled carbon nanotubes. In (b) “ L^* ” is the current maximal radius of the rotating part, which is not greater than “ L ”, the distance between the probe tip and the axis of the rotor. In the present study, $L \geq L^* + 0.142$ nm. Detailed parameters are listed in Table 1.

Table 1 Parameters of the system shown in Fig. 1 (unit of length: nm)

Component	Motor		Wing		Probe	
Name of part	Rotor	Stator	HGN	End-tube	Inner tube	Outer tube
Chirality	(9, 9)	(14, 14)	(\times , \times)	(5, 5)	(5, 5)	(10, 10)
Length (direction)	8.116 (z)	0.492 (z)	4.181 (z)	4.673 (z)	5.682 (y)	6.026 (y)
Diameter/width	1.220	1.898	8.378 (x)	0.678	0.678	1.356
Number of atoms	1206C	140C	1400C + 80H ^a	390C + 20H	470C	990C

^a Note: the number of hydrogen atoms bonded with the inner carbon atoms on HGN is not involved.

due to thermal-vibration-caused collision between the rotor and stators. The rotor can be driven to rotate as the amplitude of thermal vibration of the atoms on the rotor is high enough, *e.g.*, >100 K, and the IRD is higher than 0.1 time of 0.142 nm. More details can be found in ref. 27. Simultaneously, 300 K is a room temperature rather than ultra-low or high temperature. This is the reason we choose 300 K in the present study.

To describe the interaction among carbon and hydrogen atoms in the system, the Adaptive Intermolecular Reactive Empirical Bond Order (AIREBO) Potential proposed by Stuart *et al.*²⁹ is employed. The potential function contains three terms, *i.e.*,

However, after 384 ps, the wing with $N_t = 2$ becomes flat, indicating that the unstable configuration plays only a small role in the acceleration process. The upper part of Fig. 2b demonstrates that, due to the periodic curvature of the wing along the radial direction, the wing with $N_t = 2$ has a longer duration of oscillation along the radial direction, *i.e.*, 5000 ps. Only after 7376 ps, the VPE becomes positive, which means that the wing with $N_t = 2$ has the same length as that of the wing with $N_t = 0$ in the initial state. From then on, the system collapses after 6324 ps (=13 700–7376 ps), which is very close to the length of interval [1856, 8000] ps for the wing with $N_t = 0$. The reason is

$$\left\{ \begin{array}{l} P = P_{REBO} + P_{Torsion} + P_{L-J} \\ P_{REBO} = \sum_i \sum_{j(j>i)} \left[V_{ij}^R(r_{ij}) - b_{ij} V_{ij}^A(r_{ij}) \right] \\ P_{Torsion} = \frac{1}{2} \sum_i \sum_{j(j \neq i)} \sum_{k(k \neq i,j)} \sum_{l(l \neq i,j,k)} w_{ij}(r_{ij}) \cdot w_{jk}(r_{ij}) \cdot w_{kl}(r_{ij}) \cdot V_{Torsion}(\omega_{ijkl}) \\ P_{L-J} = \sum_i \sum_{j(j>i)} 4\epsilon \left[\left(\frac{\sigma}{r_{ij}} \right)^{12} - \left(\frac{\sigma}{r_{ij}} \right)^6 \right] \end{array} \right. \quad (1)$$

where P_{REBO} is the short-range REBO potential in which V_{ij}^R and V_{ij}^A are repulsive and attractive pairwise potentials determined by the atom types of atoms i and j . r_{ij} is the distance between atoms i and j , and b_{ij} is the many-body term. $P_{Torsion}$ is a term dependent on the dihedral angle ω of the atoms i, j, k , and l , in which the bond weight w_{ij} is in [0, 1], and $V_{Torsion}$ is the atom-based dihedral-angle potential. P_{L-J} describes the non-bonded intermolecular interactions (L-J interaction), in which $\sigma_{C-C} = 0.34$ nm, $\sigma_{H-H} = 0.265$ nm, $\sigma_{C-H} = (\sigma_{C-C} + \sigma_{H-H})/2$, $\epsilon_{C-C} = 2.84$ meV, $\epsilon_{H-H} = 1.5$ meV, $\epsilon_{C-H} = 1.376$ meV, and the cutoff is 1.02 nm.

3. Results and discussion

3.1 Effect of hydrogenation on GN in the system without the probe

Fig. 2a shows the rotational histories of the wing with ($N_t = 2$) and without hydrogenation ($N_t = 0$). Before approaching the maximum rotational frequency of ~49 GHz, the acceleration duration of the wing with $N_t = 0$, *i.e.*, 8000 ps, is shorter than that of the wing with $N_t = 2$, *i.e.*, 13 700 ps. One of the reasons is that the configuration of the wing with $N_t = 2$ in the initial stage is less stable than that of the wing with $N_t = 0$. For example, the configurations of the two wings at 21 ps are different.

that the rotor with plate wing $N_t = 2$ has the same moment of inertia. Hence, the two rotors need approximately the same length of acceleration duration to have the critical rotational speed of collapse. Hence, a wing with a spring character can increase the duration of acceleration of the wing.

From the upper part of Fig. 2b, we can find that the variation of the wing with $N_t = 0$ is about 0.6 nm before breakdown (due to the centrifugal force of the rotating part on the rotor), while the length of the wing with $N_t = 2$ varies from 9 to 10.5 during rotational acceleration before breakdown. Although the two wings have the same peak value of L^* , the length of the wing with $N_t = 2$, *i.e.*, L^* , displays greater variation than that of the wing with $N_t = 0$. This is an important characteristic for the measurement of the rotation of the wing.

From Fig. 2a, we know that the system is unstable if the rotational acceleration of the wing has no constraint. In the following discussion, the system includes a probe that is located near the track of the end-tube.

3.2 Effect of L on the stable rotational frequency of HGN

To show the effect of the length of HGN on the rotational frequency, the distance between the probe tip and the rotating axis of the rotor is set to be four different values for each

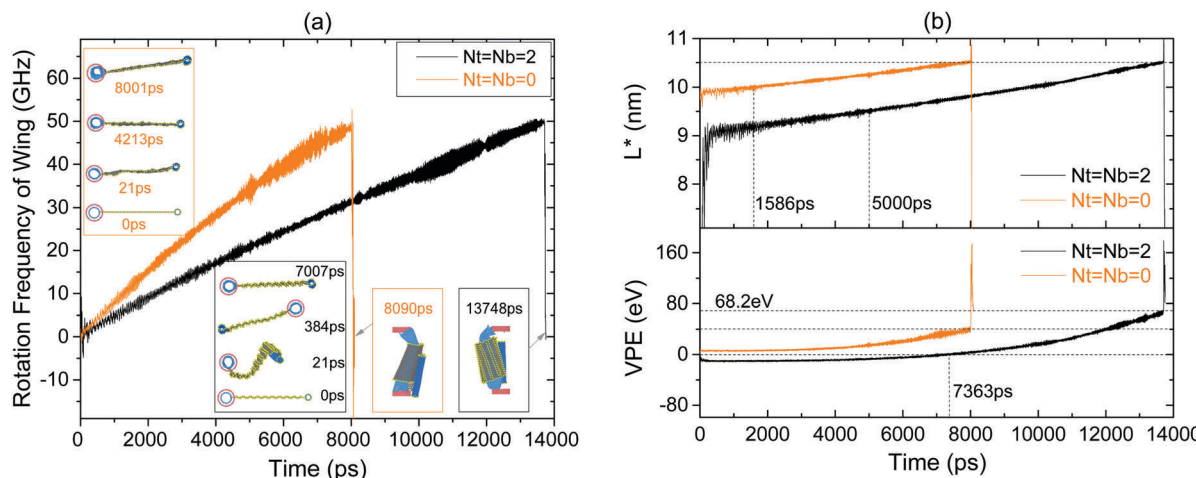


Fig. 2 The dynamic responses of the two rotary systems without a probe. The basic data of the systems are the same as listed in Table 1, but the hydrogenation schemes are different, i.e., $N_t = N_b = 0$ and 2, respectively. (a) The rotational frequency history of two systems; (b) the history of the maximal radius of the rotating part (L^*) and the variation history of potential energy (VPE) of systems.

hydrogenation scheme, namely, $L = 10.25, 9.9, 9.6$, and 9.4 nm for the scheme of $N_t = 2$ and $L = 10.5, 10.1, 9.5$, and 8.8 nm for the scheme of $N_t = 4$. For the ideal rotating part, whose HGN is flat and not deformed, $L^* = L - 0.142$ nm. Hence, L^* is larger or HGN has greater length when L is larger.

In Fig. 3a, the final stable rotational frequency of the wing approaches 37.49, 28.68, 18.80, and 9.13 GHz for the length of L being 10.25, 9.9, 9.6, and 9.4 nm, respectively. Clearly, the stable rotational frequency varies monotonously with respect to the length of HGN (or L). Simultaneously, the rotating part is driven by the same stators, and a rotating part with longer HGN means that the part has a higher moment of inertia. Hence, the longer rotating part needs more time to arrive at the stable rotational state. In Fig. 3b, the rotational acceleration lasts 8800 ps when $L = 10.25$ or L^* reaches 10.108 nm. When $L = 9.4$ nm, the acceleration process needs only 3200 ps.

If the wing has a different hydrogenation scheme, e.g., $N_t = 4$, the stable rotational frequency is still higher with respect to the higher value of L , e.g., 42.41 GHz vs. 10.5 nm or 12.49 GHz vs. $L = 8.8$ nm. If we compare the two groups of rotational histories shown in Fig. 3a and c, we find that the maximal rotational frequency (f) has a linear relationship with the length of rotating part (or L), rather than with the hydrogenation schemes. The relationship between the L and the stable rotational frequency of the system can be obtained as

$$\begin{cases} L = 9.083 + 0.030f & \text{for } (N_t = N_b = 2) \\ L = 8.146 + 0.057f & \text{for } (N_t = N_b = 4) \end{cases} \quad (2)$$

Moreover, due to the centrifugal effect, the length of the rotating part increases with the increase in rotational frequency. Comparisons among the results in Fig. 3b and d show that the variation in the length of the wing with $N_t = 2$ is much smaller than that of the wing with $N_t = 4$. Currently, the time for the length of a wing to become stable is 8700 ps when $L = 10.5$ nm with respect to $N_t = 4$. Hence, when $L < 10.5$ nm, e.g., 10.25 nm, the acceleration process requires more than 8700 ps.

The other cases are similar. The conclusion can be drawn, therefore, that the duration of the acceleration process (t_a) of the wing with $N_t = 4$ is shorter than that of the wing with $N_t = 2$ when the wings have the same length. The relationship between L and the time of the acceleration process can be obtained, e.g.,

$$\begin{cases} L = 8.872 + 1.471t_a & \text{for } (N_t = N_b = 2) \\ L = 8.368 + 2.456t_a & \text{for } (N_t = N_b = 4) \end{cases} \quad (3)$$

Comparison of the fluctuation of L^* with respect to different values of L (in Fig. 3b and d) shows that the amplitude of fluctuation of L^* decreases with the increase of L . This finding indicates that the system is in a higher stable state during rotation when the length of HGN is greater. That phenomenon is important for the design of a system for measuring the rotational speed of a rotor.

When $N_t = 4$ and $L = 9.5$ nm, the system breaks down at 9600 ps. The reason is that the rotor has an axial oscillation which leads to the escape of the rotor from the short stators. Due to the unsaturated carbon atoms on the ends of tubes, the rotor and a stator are bonded together, which is similar to the inset with respect to 8090 ps in Fig. 2a. Providing longer stators in the system can avoid this problem.

In a stable rotary system, the acceleration of the rotor must be constrained by the probe tip through collision. Theoretically, when the probe tip is near the track of the end-tube, collision occurs when the wing becomes flat due to the centrifugal force. However, this premise is based on the condition that the wing features no twist.

In Fig. 4, two cases are shown for each hydrogenation scheme. From the snapshots of the system along the rotating axial direction (z -direction) inserted in Fig. 4a and b, the end-tube has slight twist in the initial stage, here, 3311 ps in Fig. 4a and 3054 ps in Fig. 4b. Hence, the rotation becomes stable after a period of acceleration. However, the wing has a marked twist when $N_t = 4$. From Fig. 4c and d, we find that the twist is common. Moreover, due to the wing twist, the acceleration of rotation

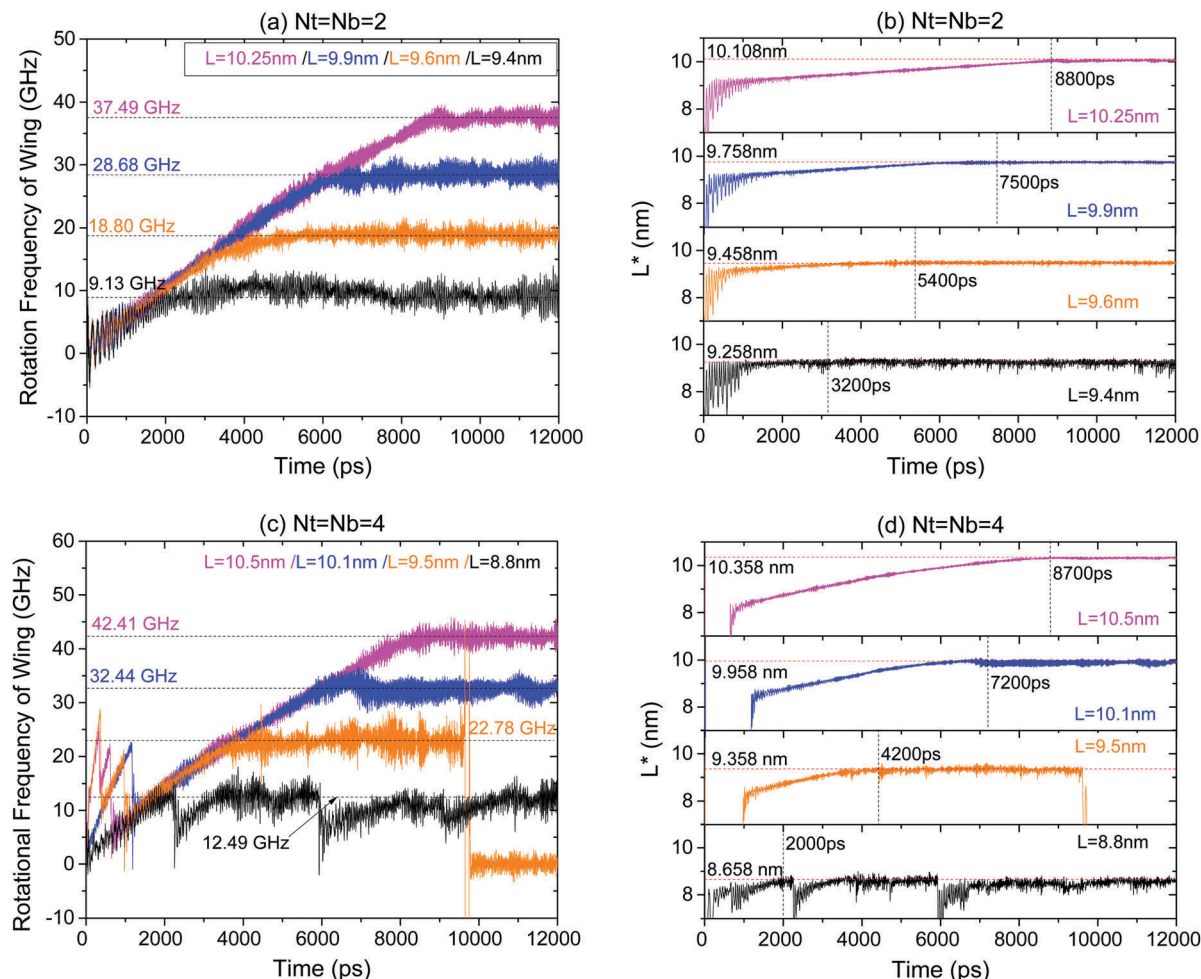


Fig. 3 The dynamic response of the rotating part in the system with different lengths of HGN. (a) The rotational frequencies of the wing with $N_t = 2$. (b) The maximal lengths of the rotating part (L^*) with $N_t = 2$. (c) The rotational frequency of the wing with $N_t = 4$. (d) The maximal lengths of the rotating part (L^*) with $N_t = 4$.

is not stable. In Fig. 4c, for example, the rotational frequency of the wing shows three instances of obvious decrease, near 2266 ps, 5927 ps, and 9000 ps (Movie 1, ESI†). In Fig. 4d, the rotational frequency shows dramatic fluctuation in the first 1000 ps (Movie 2, ESI†). The dramatic variation of the wing rotation is due to two causes. One is that the middle part of the wing is attracted to the rotor during rotation, leading to obvious variation of the moment of inertia of the rotating part. The other cause is that the wing curves and shrinks from the initial flat state from the freed end (end-tube) to the rotor. That wing shrinkage results in a collision of the wing against the rotor. Obviously, although the phenomenon appears just in the case of $L = 10.5$ (with $N_t = 4$) as shown in Fig. 4d, it occurs commonly as shown in Fig. 3c.

In Fig. 4c, the three jumps in rotational frequency reflect different causes. For the first jump, the cause is given above. For the next two jumps, the cause is collision between the end-tube and probe tip. It is known that a wing twist reduces the width of the trace of the end-tube during rotation. Therefore, the chance of collision between the end-tube and probe tip is also reduced. At the same time, however, the maximal radius of

the rotating part (L^*) increases. If any collision occurs, that between the twisted end-tube and probe tip will be stronger than that between the non-twisted end-tube and probe tip. From the foregoing, we know that a stronger collision means higher energy transfer from the end-tube to probe tip. The end-tube experiences a sharp decrease in velocity, indicating that it is not rotating synchronously with the HGN. The configuration of the wing can be found from the snapshots at 5927 ps and 5946 ps in Fig. 4c.

From comparisons of the wing twists with different values of N_t , it is evident that the twist angle of the end-tube increases with an increase in the value of N_t . To avoid failure of collision between the end-tube and probe tip, an end-tube with a 90° twist angle should be avoided. In the next section, the effect of N_t is discussed.

3.3 Effect of N_t on the configuration of HGN

Fig. 5 shows the system configurations obtained by relaxing the initial flat wing at a canonical NVT ensemble with $T = 8$ K followed by a temperature increase to 300 K. In the system,

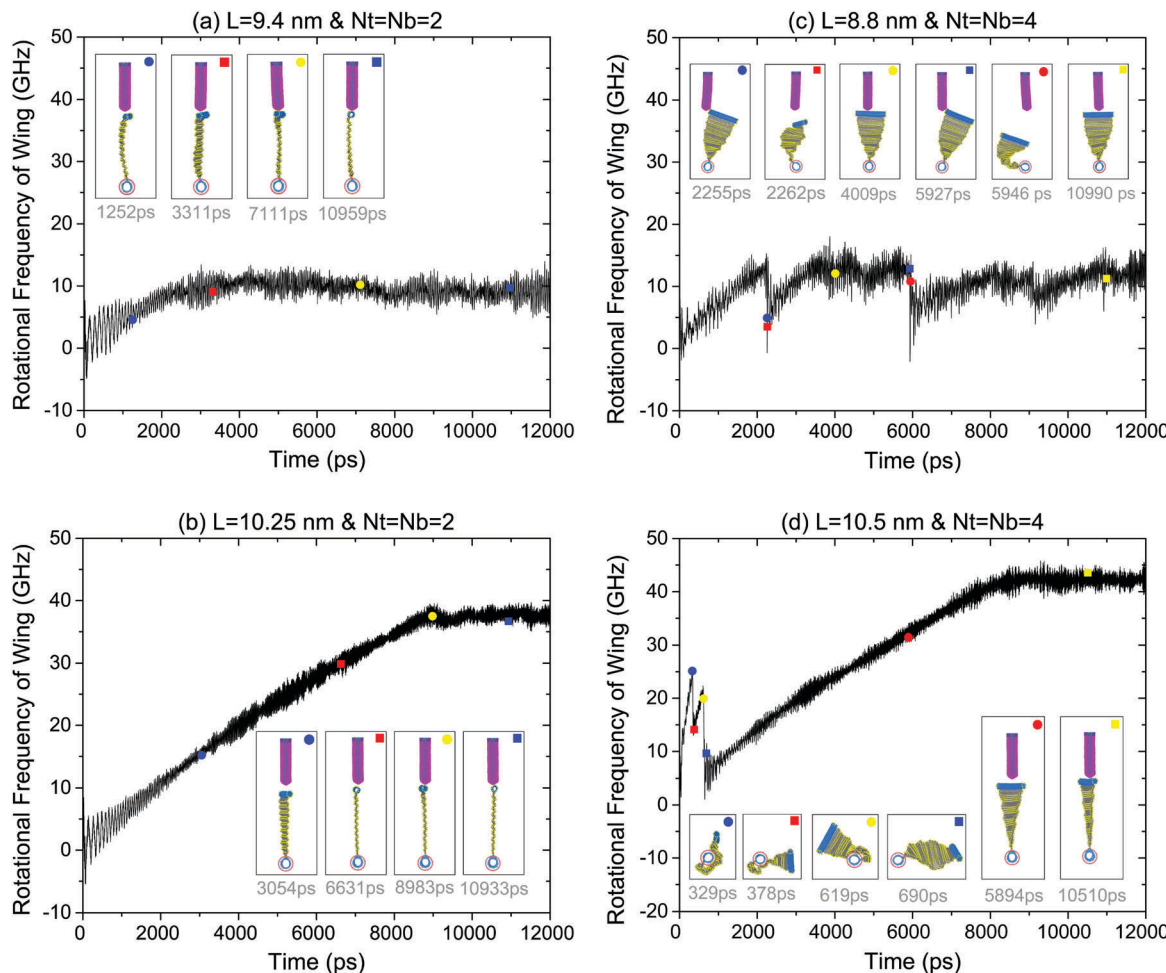


Fig. 4 Representative configurations of the wing during acceleration and collision with the probe tip when the systems have different HGNs. (a) $L = 9.4 \text{ nm}$ and $N_t = 2$. (b) $L = 10.25 \text{ nm}$ and $N_t = 2$. (c) $L = 8.8 \text{ nm}$ and $N_t = 4$. (d) $L = 10.5 \text{ nm}$ and $N_t = 4$.

the length of HGN is 24.14 nm. The hydrogenation schemes of the GN are at $N_t = 5, 10, 15, 16, 20$, and 25, respectively.

It can be seen that the wing features a spring when N_t is not greater than 16. The four configurations have similar aspects, *e.g.*, the neighboring C-H sides of the HGN attract each other, reducing the potential energy of the system, and the wing is nearly symmetric about the central cross-section of the rotor. The difference between the configurations in Fig. 5c and d is that the middle part of the wing is attracted to the rotor and the end-tube is attracted to the middle part when $N_t = 16$. This observation indicates that the configuration of the wing will change further if N_t is greater than 16. For example, with $N_t = 20$ or 25, the wing has a complex configuration that features curving, twisting, and folding. The asymmetry of such a wing easily results in unstable oscillation of the wing along the axial direction (z -direction), which should be avoided while measuring the rotation.

As we study the ratio between the length of each hydrogenation area (N_t times 0.213 nm) and the width of HGN (*i.e.*, $W = 4.379 \text{ nm}$), we find that the ratios are 0.19 ($N_t = 5$), 0.44 ($N_t = 10$), 0.68 ($N_t = 15$), 0.73 ($N_t = 16$), 0.93 ($N_t = 20$),

and 1.17 ($N_t = 25$), respectively. These findings suggest that complex configurations of the wing can be avoided if the ratio is no greater than 0.73.

The above discussion focuses on the dynamic behaviors of the wing in rotation. Our major aim is to measure the rotational frequency of the rotor through the dynamic response of the probe tip. The next section provides the related discussion.

3.4 Deflection of the probe tip vs. rotational frequency of HGN

After our investigation of the behavior of the wing on the rotor, the dynamic response of the probe is discussed here. In Fig. 6, the deflection of the probe tip along the x -direction is shown, indicating that the maximal deflection of the probe tip is lower when L is higher, *e.g.*, 0.096 nm when $L = 10.25 \text{ nm}$ and 0.406 nm when $L = 9.4 \text{ nm}$, in the system with $N_t = 2$. If $N_t = 4$, the maximal deflection of the probe tip is higher than that of the probe tip colliding with the wing with $N_t = 2$. As we compare the deflection of the probe tip in Fig. 6 and the rotational behavior of the wing in Fig. 3, we find that the tip deflection is approximately inversely proportional to the rotational frequency of the wing (or the velocity of the end-tube). The results derive from our perception

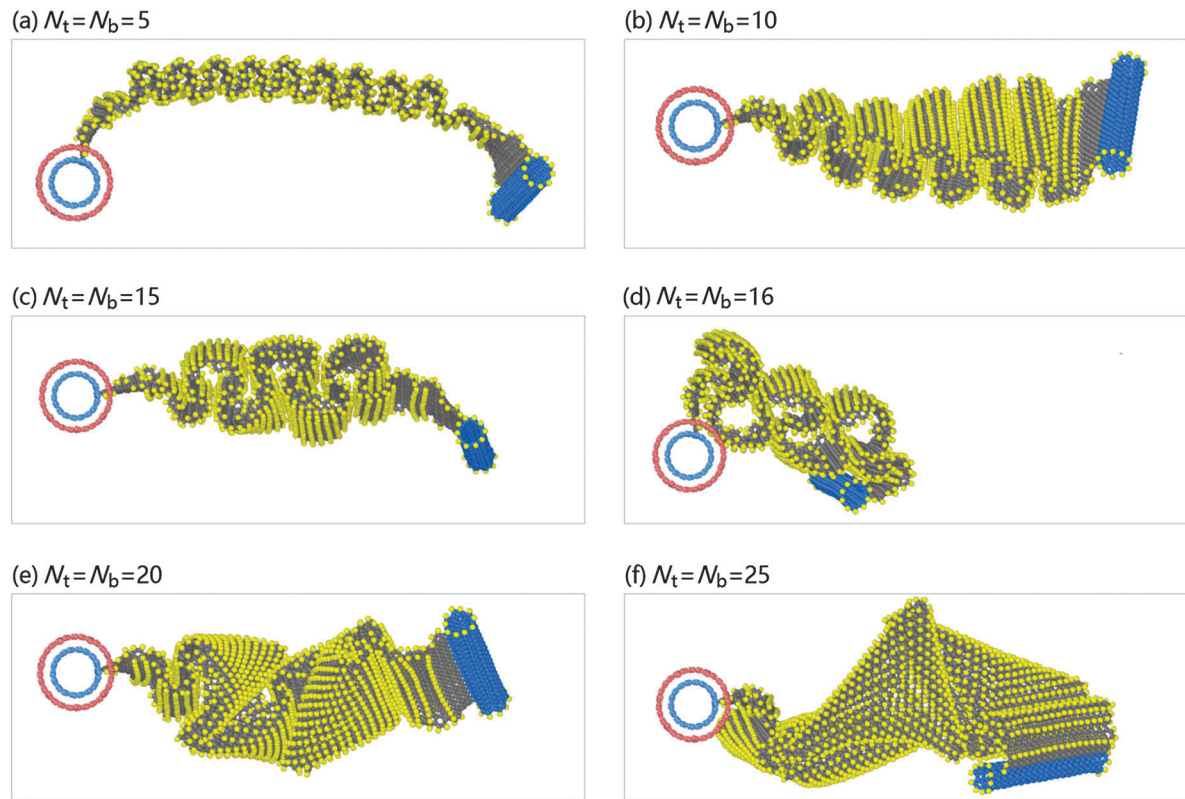


Fig. 5 Relative stable configurations of the wing with different hydrogenation schemes after full relaxation.

but do not reveal the mechanism. Intuitively, collision with an end-tube with higher velocity should lead to greater deflection of the probe tip due to greater energy transmission during collision. But the results give an opposite answer.

It is known that energy transmission from the end-tube to the probe depends on two factors. One is the relative position of the end-tube and the probe tip during collision: the smaller the distance between the end-tube and probe tip, the higher the repulsive force between them. The distance depends on the fluctuation of L^* near the value of $(L - 0.142)$ nm (the initial ideal length of the rotating part). From Fig. 3b ($N_t = 2$), we find that the fluctuation of L^* with respect to $L = 9.4$ nm (black curve) is far greater than that of L^* with respect to $L = 10.25$ nm (pink curve). And the interaction between the end-tube and probe tip is expressed using L-J potential (eqn (1)). Hence, when the L^* is greater than $L - 0.142$ nm, the interaction increases dramatically. Due to the greater fluctuation of L^* with respect to $L = 9.4$ nm, the exclusive force must be higher than that between the end-tube and probe tip when $L = 10.25$ nm (Movie 3 and 4, ESI†). The second factor is the duration of the collision process. As the two systems with respect to L have the same end-tube and probe, the duration of the collision process is inversely proportional to the velocity of the end-tube. The velocity can be obtained by the product of the rotational frequency of the wing and the length of the rotating part. From Fig. 3a, we know that the velocity of the end-tube with respect to $L = 10.25$ nm is much higher than that of the end-tube with respect to $L = 9.4$ nm. Hence, the duration of interaction

between the end-tube and probe when $L = 9.4$ nm is also greater than that with respect to $L = 10.25$ nm. By virtue of the weaker repulsion and shorter duration of collision with respect to a longer rotating part, the probe tip attracts lower energy from the end-tube. Hence, the maximal deflection of the probe tip (or d_p) is smaller when L is higher. This conclusion remains when N_t changes, e.g., $N_t = 4$. The relation between L and the maximal deflection of the probe tip can be given as

$$\begin{cases} d_p = \frac{8.880}{L^{0.055}} & \text{for } (N_t = N_b = 2) \\ d_p = \frac{8.754}{L^{0.075}} & \text{for } (N_t = N_b = 4) \end{cases} \quad (4)$$

Substituting eqn (2) into eqn (4), the relationship between d and rotational speed can be obtained:

$$\begin{cases} d_p = \frac{8.880}{(9.083 + 0.030f)^{0.055}} & \text{for } (N_t = N_b = 2) \\ d_p = \frac{8.754}{(8.146 + 0.057f)^{0.075}} & \text{for } (N_t = N_b = 4) \end{cases} \quad (5)$$

To reflect the rotation of the rotor, generally, a probe with higher deflection should be adopted in the system. That means that the length of the wing should be controlled within a range that takes into account both the deflection of the probe tip and the stability of rotational frequency of the rotor.

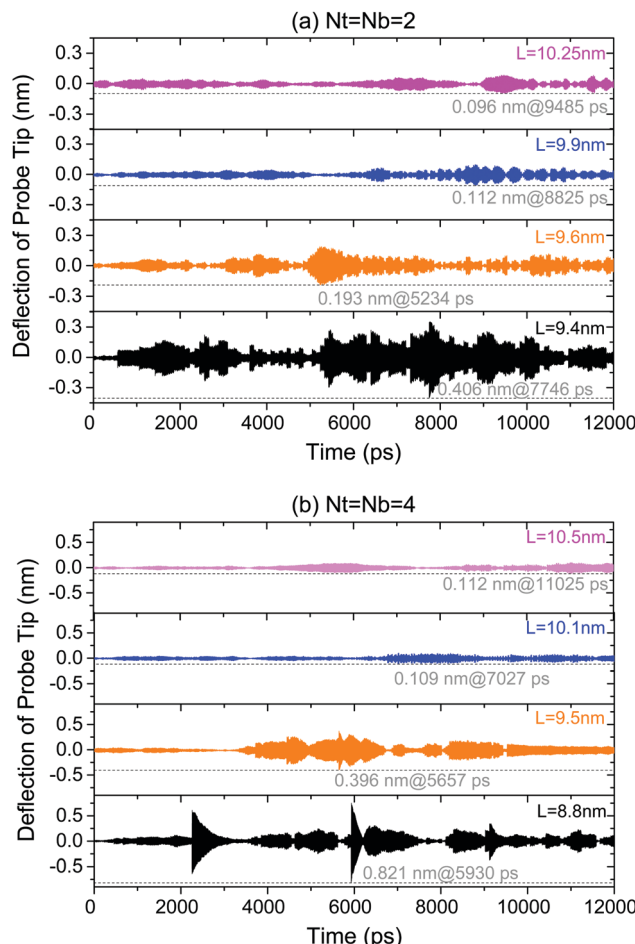


Fig. 6 History of the deflection of the probe tip (along x-axis) with different values of L in systems with different N_t .

4. Conclusions

To illustrate the effect of hydrogenation schemes on the dynamics of a system for measuring the rotation of a thermally driven rotary nanomotor made from carbon nanostructures, the rotor is connected to an end-tube with a GN whose two surfaces are hydrogenated differently. Also, the effect of the length of the wing (HGN + end-tube) is discussed. From numerical experiments, some conclusions can be drawn that are relevant to potential application for measuring the rotational frequency of a rotor.

(1) In a given system without a probe, in comparison with a wing with $N_t = 0$ (the GN not being hydrogenated), the wing takes longer to reach the maximal rotational frequency when the GN in the wing is hydrogenated ($N_t > 0$).

(2) In systems with the same hydrogenation scheme, the stable rotational frequency of the rotor is higher if the rotor and end-tube are connected to a longer GN. The length of the rotating part with a shorter GN fluctuates more obviously than that of the part with a longer GN.

(3) In systems with the same length of GN, when the ratio of the width of each hydrogenated area to the width of GN is greater than 0.73, the wing has a complex configuration due to

the GN being curved, twisted, and folded to reduce the potential energy. A wing with such complex configuration easily creates oscillation along the axis of the rotor, which should be avoided when measuring the rotation of the rotor.

(4) In systems with a longer hydrogenated GN, the maximal deflection of the probe tip (which is initially 0.142 nm from the track of the end-tube) is lower when it collides with the end-tube on the free end of the GN. To ensure an obvious deflection of the probe tip, one can use a shorter wing or move the probe closer to the track of the end-tube.

Acknowledgements

The authors are grateful for the financial support from the National Natural Science Foundation of China (Grant No. 11502217, 11372100) and the Australian Research Council (Grant No. DP140103137).

References

- 1 S. Iijima, Helical Microtubules of Graphitic Carbon, *Nature*, 1991, **354**, 56–58.
- 2 K. S. Novoselov, A. K. Geim, S. Morozov, D. Jiang, Y. Zhang, S. a. Dubonos, I. Grigorieva and A. Firsov, Electric Field Effect in Atomically Thin Carbon Films, *Science*, 2004, **306**, 666–669.
- 3 A. A. Balandin, S. Ghosh, W. Bao, I. Calizo, D. Teweldebrhan, F. Miao and C. N. Lau, Superior Thermal Conductivity of Single-Layer Graphene, *Nano Lett.*, 2008, **8**, 902–907.
- 4 C. Lee, X. Wei, J. W. Kysar and J. Hone, Measurement of the Elastic Properties and Intrinsic Strength of Monolayer Graphene, *Science*, 2008, **321**, 385–388.
- 5 W. Qiu, Q. Li, Z. K. Lei, Q. H. Qin, W. L. Deng and Y. L. Kang, The Use of a Carbon Nanotube Sensor for Measuring Strain by Micro-Raman Spectroscopy, *Carbon*, 2013, **53**, 161–168.
- 6 K. Cai, H. Cai, J. Shi and Q. H. Qin, A Nano Universal Joint Made from Curved Double-Walled Carbon Nanotubes, *Appl. Phys. Lett.*, 2015, **106**, 241907.
- 7 K. Cai, H. Cai, L. Ren, J. Shi and Q. H. Qin, Over-Speeding Rotational Transmission of a Carbon Nanotube-Based Bearing, *J. Phys. Chem. C*, 2016, **120**, 5797–5803.
- 8 J. Cumings and A. Zettl, Low-Friction Nanoscale Linear Bearing Realized from Multiwall Carbon Nanotubes, *Science*, 2000, **289**, 602–604.
- 9 R. Zhang, Z. Ning, Y. Zhang, Q. Zheng, Q. Chen, H. Xie, Q. Zhang, W. Qian and F. Wei, Superlubricity in Centimetres-Long Double-Walled Carbon Nanotubes under Ambient Conditions, *Nat. Nanotechnol.*, 2013, **8**, 912–916.
- 10 K. Mukai, K. Asaka, T. Sugino, K. Kiyohara, I. Takeuchi, N. Terasawa, D. N. Futaba, K. Hata, T. Fukushima and T. Aida, Highly Conductive Sheets from Millimeter-Long Single-Walled Carbon Nanotubes and Ionic Liquids: Application to Fast-Moving, Low-Voltage Electromechanical Actuators Operable in Air, *Adv. Mater.*, 2009, **21**, 1582–1585.

- 11 W. Qiu, Y. L. Kang, Z. K. Lei, Q. H. Qin and Q. Li, A New Theoretical Model of a Carbon Nanotube Strain Sensor, *Chin. Phys. Lett.*, 2009, **26**, 080701.
- 12 K. Jensen, K. Kim and A. Zettl, An Atomic-Resolution Nanomechanical Mass Sensor, *Nat. Nanotechnol.*, 2008, **3**, 533–537.
- 13 W. Qiu, Y. L. Kang, Z. K. Lei, Q. H. Qin, Q. Li and Q. Wang, Experimental Study of the Raman Strain Rosette Based on the Carbon Nanotube Strain Sensor, *J. Raman Spectrosc.*, 2010, **41**, 1216–1220.
- 14 A. Rinaldi, S. Licoccia and E. Traversa, Nanomechanics for Mems: A Structural Design Perspective, *Nanoscale*, 2011, **3**, 811–824.
- 15 X. Zang, Q. Zhou, J. Chang, Y. Liu and L. Lin, Graphene and Carbon Nanotube (Cnt) in Mems/Nems Applications, *Micro-electron. Eng.*, 2015, **132**, 192–206.
- 16 A. Barreiro, R. Rurali, E. R. Hernandez, J. Moser, T. Pichler, L. Forro and A. Bachtold, Subnanometer Motion of Cargoes Driven by Thermal Gradients Along Carbon Nanotubes, *Science*, 2008, **320**, 775–778.
- 17 H. A. Zambrano, J. H. Walther and R. L. Jaffe, Thermally Driven Molecular Linear Motors: A Molecular Dynamics Study, *J. Chem. Phys.*, 2009, **131**, 241104.
- 18 S. Legoas, V. Coluci, S. Braga, P. Coura, S. Dantas and D. Galvao, Molecular-Dynamics Simulations of Carbon Nanotubes as Gigahertz Oscillators, *Phys. Rev. Lett.*, 2003, **90**, 055504.
- 19 K. Cai, H. Yin, Q. H. Qin and Y. Li, Self-Excited Oscillation of Rotating Double-Walled Carbon Nanotubes, *Nano Lett.*, 2014, **14**, 2558–2562.
- 20 A. Fennimore, T. Yuzvinsky, W. Q. Han, M. Fuhrer, J. Cumings and A. Zettl, Rotational Actuators Based on Carbon Nanotubes, *Nature*, 2003, **424**, 408–410.
- 21 J. W. Kang and H. J. Hwang, Nanoscale Carbon Nanotube Motor Schematics and Simulations for Micro-Electro-Mechanical Machines, *Nanotechnology*, 2004, **15**, 1633–1638.
- 22 Z. Tu and X. Hu, Molecular Motor Constructed from a Double-Walled Carbon Nanotube Driven by Axially Varying Voltage, *Phys. Rev. B: Condens. Matter Mater. Phys.*, 2005, **72**, 033404.
- 23 B. Wang, L. Vuković and P. Král, Nanoscale Rotary Motors Driven by Electron Tunneling, *Phys. Rev. Lett.*, 2008, **101**, 186808.
- 24 A. Prokop, J. Vacek and J. Michl, Friction in Carborane-Based Molecular Rotors Driven by Gas Flow or Electric Field: Classical Molecular Dynamics, *ACS Nano*, 2012, **6**, 1901–1914.
- 25 M. Hamdi, A. Subramanian, L. Dong, A. Ferreira and B. J. Nelson, Simulation of Rotary Motion Generated by Head-to-Head Carbon Nanotube Shuttles, *Mechatronics, IEEE/ASME Transactions*, 2013, **18**, 130–137.
- 26 K. Cai, Y. Li, Q. H. Qin and H. Yin, Gradientless Temperature-Driven Rotating Motor from a Double-Walled Carbon Nanotube, *Nanotechnology*, 2014, **25**, 505701.
- 27 K. Cai, J. Wan, Q. H. Qin and J. Shi, Quantitative Control of a Rotary Carbon Nanotube Motor under Temperature Stimulus, *Nanotechnology*, 2016, **27**, 055706.
- 28 S. Plimpton, Fast Parallel Algorithms for Short-Range Molecular Dynamics, *J. Comput. Phys.*, 1995, **117**, 1–19.
- 29 S. J. Stuart, A. B. Tutein and J. A. Harrison, A Reactive Potential for Hydrocarbons with Intermolecular Interactions, *J. Chem. Phys.*, 2000, **112**, 6472–6486.
- 30 S. Zhu and T. Li, Hydrogenation-Assisted Graphene Origami and Its Application in Programmable Molecular Mass Uptake, Storage, and Release, *ACS Nano*, 2014, **8**, 2864–2872.